Chapter 11
Nanoscale Testing of One-Dimensional Nanostructures

B. Peng, Y.G. Sun, Y. Zhu, H.-H. Wang, and H.D. Espinosa

AQ: Please expand
Author's initials.

11.1 Introduction

The emergence of numerous nanoscale materials and structures such as nanowires (NWs), nanorods, nanotubes, and nanobelts of various materials in the past decade has prompted a need for methods to characterize their unique mechanical properties. These one-dimensional (1D) nanostructures possess superior mechanical properties [1, 2]; hence, applications of these structures ranging from nanoelectromechanical systems (NEMS) [3] to nanocomposites [4] are envisioned.

Two overarching questions have spurred the development of nanomechanical testing techniques and the modeling of materials behavior at the nanoscale: how superior is material behavior at the nanoscale as compared to its bulk counterpart, and what are the underlying mechanisms that dictate this? Due to the limited number of atoms present in these nanostructures, they provide an excellent opportunity to couple experimentation and atomistic modeling on a one-to-one basis. This approach has the potential to greatly advance our understanding of material deformation and failure, as well as to validate the various assumptions employed in multiscale models proposed in the literature. A large number of atomistic simulations have been performed to predict nanostructure properties and reveal their deformation mechanisms [2]. However, due to the minute scale of these nanostructures, it has proven quite challenging to conduct well-instrumented mechanical testing and validate computational predictions.

Earlier nanomechanical testing techniques include thermally- or electrically-induced vibration of cantilevered nanostructures inside a transmission electron microscope (TEM) [5, 6]; lateral bending of suspended nanostructures using an

B. Peng, Y. Zhu, and H.D. Espinosa

Mechanical Engineering, Northwestern University, 2145 Sheridan Rd., Evanston, IL 60208-3111
bpeng@northwestern.edu, espinosa@northwestern.edu

Y.G. Sun and H.-H. Wang
Argonne National Laboratory, Argonne, IL 60439

AQ: Please provide
Email address for
Author "Y. Zhu,
Y.G. Sun and H.-H.
Wang".

atomic force microscope (AFM) [7, 8]; radial compression, by means of atomic force microscopy (AFM) probes, or nanoindentation of nanostructures on substrates [9, 10]; and tensile testing of freestanding nanostructures between two AFM cantilevers within a scanning electron microscope (SEM) [11]. Despite the exciting progress achieved by these methods, they are in general not well controlled in terms of loading, boundary conditions, and force–displacement measurements. In some instances, the nanostructure properties must be inferred from assumed models of the experimental setup.

Recent advances in mechanical characterization of thin films have been remarkable and provide good insight for the testing of nanostructures. Among numerous techniques, two categories are particularly fascinating: in situ testing and on-chip testing. In situ testing provides a powerful means to obtain the deformation field and to observe the deformation mechanisms though real-time imaging, for example, by SEM. The SEM chamber is large enough to accommodate a microscale testing setup, and has been used for in situ tensile testing [12,13]. Another example of in situ testing involves an AFM to record the surface profile during a tensile test [14]. TEM is ideal for in situ testing since it provides direct evidence of the defects nucleation and reaction. Although most in situ TEM setups do not measure or control stresses in the specimen [15, 16], Haque and Saif recently incorporated a load sensor in the TEM [17, 18]. An on-chip testing system consists of micromachined elements, such as comb-drive actuators and force (load) sensors that can be integrated on a chip. One of the early attempts used electrostatic actuation and sensing for fatigue testing of silicon cantilever beams [19]. Osterberg and Senturia used electrostatic actuation for chip-level testing of cantilever beams, fixed–fixed beams, and clamped circular diaphragms to extract material properties [20]. Kahn et al. [21] used electrostatic actuators integrated with microfracture specimens to study fracture properties of polysilicon films. Owing to the capability of generating and measuring small-scale forces and displacements with high resolution, on-chip testing has the potential to impact the small-scale testing field profoundly. Note that these two concepts, in situ and on-chip, are related but different. On-chip testing can be performed in situ or ex situ. In situ testing does not necessarily utilize an on-chip device. But due to the small size of on-chip devices and integrated loading and force sensing capabilities, they conveniently facilitate in situ testing.

In this chapter, the nanomechanical characterization of 1D nanostructures is reviewed. In Sect. 11.2, we summarize the challenges for mechanical characterization of 1D nanostructures. In Sect. 11.3, an overview of the existing experimental techniques is presented. In Sect. 11.4, a newly developed nanoscale material testing system for characterizing nanostructures is described in detail. In Sect. 11.5, some experimental results [22,23] are summarized with emphasis on the in situ electromechanical testing of nanostructures, which complements our nanomechanical testing.

11.2 Challenges for Mechanical Characterization of 1D Nanostructures

The proper measurement of loads and displacements applied to 1D nanostructures, such as NWs and CNTs, is extremely challenging because of the miniscule size. Earlier studies on mechanical properties of nanostructures focused on theoretical analyses and numerical simulations [2, 24]. Owing to advancement in various microscopic techniques, nanoscale experimental tools have been developed to exploit the capabilities of high-resolution microscopes. Major challenges in the experimental study of 1D nanostructures include (1) constructing appropriate tools to manipulate and position specimens; (2) applying and measuring forces with nano-Newton resolution; and (3) measuring local mechanical deformation with subnanometer resolution.

11.2.1 Manipulation and Positioning

The first important step in testing is to manipulate and position the nanostructures at the desired location with nanometer resolution. For tensile testing, this becomes even more challenging, as the specimens must be freestanding and clamped at both ends. Furthermore, they should be well-aligned with the tensile direction. In the following section, we review the available methods to mount the specimens meeting the requirements for the tensile tests.

11.2.1.1 Random Dispersion

After purification, a small aliquot of the nanostructure suspension is dropped onto the gap between two surfaces. By random distribution, some of the nanostructures are suspended across the gap with random orientation. After an appropriate nanostructure is identified, a technique called electron-beam-induced deposition (EBID) is then used to fix the two ends. This is done by depositing foreign materials [11], such as residual carbon in an SEM chamber or external precursors, such as trimethylcyclopentadienyl-platinum $(CH_3)_3CH_3C_5H_4Pt)$. Random dispersion is the simplest method for most of the mechanical testing experiments to date, but it is only modestly effective.

11.2.1.2 Nanomanipulation

AFM can be used to both image and manipulate carbon nanotubes. A "NanoManipulator" AFM system, comprising an advanced visual interface for manual control of the AFM tip and tactile presentation of the AFM data, has been developed [25].

In addition, Veeco Instruments (Woodbury, New York) developed the "NanoMan" system for high-resolution imaging, high-definition nanolithography, and direct nanoscale in-plane manipulation.

Electron microscopy provides the imaging capability for manipulation of nanostructures with nanometer resolution. Various nanomanipulators working under either SEM [11, 26] or TEM [6, 27] have been developed. These manipulators are generally composed of both a coarse micrometer-resolution translation stage and a fine nanometer-resolution translation stage, the latter being based on piezo-driven mechanisms. These manipulators typically have three linear degrees of freedom, and some even have rotational capabilities.

11.2.1.3 External Field Alignment

DC and AC/DC electric fields have been used for the alignment of nanowires [28], nanotubes [29], and bioparticles [30]. Microfabricated electrodes in close proximity are typically used to create an electric field in the gap between them. A droplet containing nanostructures in suspension is dispensed into the gap with a micropipette. The applied electric field aligns the nanostructures, due to the dielectrophoretic effect, which results in the bridging of the electrodes by a single nanostructure. Electric circuits may be used to ensure the manipulation of one single nanostructure by immediately switching off the field upon bridging (i.e., shorting of the electrodes) [30].

Huang et al. [31] demonstrated another method for aligning nanowires. A laminar flow was employed to achieve preferential orientation of nanowires on chemically patterned surfaces. Magnetic fields have also been used to align carbon nanotubes [32].

11.2.1.4 Directed Self-Assembly

Self-assembly is a method of constructing nanostructures by forming stable bonds between the organic or nonorganic molecules and substrates. Rao and colleagues [33] reported an approach in large scale assembly of carbon nanotubes with high throughput. Dip Pen Nanolithography (DPN) [34] was employed to functionalize the specific surface regions either with polar chemical groups such as amino $-NH_2/-NH_3^+$ or carboxyl $(-COOH/-COO^-)$, or with nonpolar groups such as methyl $(-CH_3)$. When the substrate with functionalized surfaces was dipped into a liquid suspension of carbon nanotubes, the nanotubes were attracted toward the polar regions and the tubes self-assembled to form predesigned structures, usually within 10 s, with a yield higher than 90%. This method is scalable to large arrays of nanotube devices by using high-throughput patterning methods such as photolithography, stamping, or massively parallel DPN.

11.2.1.5 Direct Growth

Rather than manipulating and aligning nanostructures postsynthesis, researchers also examined methods for controlled direct growth. Dai and co-workers [35, 36] reported several patterned growth approaches for CNTs. The idea is to pattern the catalyst in an arrayed fashion and control the growth of CNTs between specific catalytic sites. He et al. [37] recently succeeded in direct growth of Si nanowires between two preexisting single-crystal Si microelectrodes with <111> sidewalls. Si catalysts are deposited on the sidewalls of the electrodes and epitaxially grown perpendicularly to the <111> surfaces.

Direct growth is a very promising method to prepare specimens for nanomechanical characterization. It does not involve the nano-welding steps using EBID technique, which is advantageous because EBID brings foreign materials, e.g., carbon and platinum, onto the surface of nanostructures, which might cause some secondary effects on the property measurement. In addition, it is a rapid process, which does not require tedious manual nanomanipulation.

11.2.2 High Resolution Displacement and Force Measurements

SEM, TEM, and AFM have been widely used in characterizing nanostructures. These instruments provide effective ways of measuring dimensions and deformations with nanometer resolution. Electron microscopy uses high-energy electron beams for scattering (SEM) and diffraction (TEM). A field emission gun SEM has a resolution of about 1 nm and the TEM is capable of achieving a point-to-point resolution of 0.1–0.2 nm. The resolution of SEM is limited by the interaction volume between the electron beam and the sample surface. The resolution of TEM is limited by the spread in energy of the electron beam and the quality of the microscope optics.

Commercial force sensors usually cannot reach nano-Newton resolution. Therefore, AFM cantilevers have been effectively employed as force sensors [11, 38], provided that their spring constant has been accurately calibrated. Alternatively, microelectromechanical systems (MEMS) offer the capability to measure force with nano-Newton resolution. This MEMS-based methodology will be further discussed in Sect. 11.4.

11.3 Nanomechanical Testing of 1D Nanostructures

To date, the experimental techniques employed in the mechanical testing of 1D nanostructures can be roughly grouped into three major categories: dynamic vibration, bending, and tensile testing.

11.3.1 Dynamic Vibration

Treacy et al. [5] estimated the Young's modulus of MWNTs by measuring the amplitude of their thermal vibrations during in situ TEM imaging. The nanotubes were attached to the edge of a hole in 3-mm-diameter nickel rings for TEM observation, with one end clamped and the other free. The TEM images were blurred at the free ends, and the blurring was significantly increased with the temperature increase of the CNTs. This indicated that the vibration was of thermal origin. Blurring occurs because the vibration cycle is much shorter than the integration time needed for capturing the TEM image. The Young's modulus was estimated from the envelope of the thermal vibration.

Poncharal et al. [6] measured the Young's modulus of MWNTs by inducing mechanical resonance. The actuation was achieved utilizing an AC electrostatic field within a TEM (Fig. 11.1a). In the experiment, the nanotubes were attached to a fine
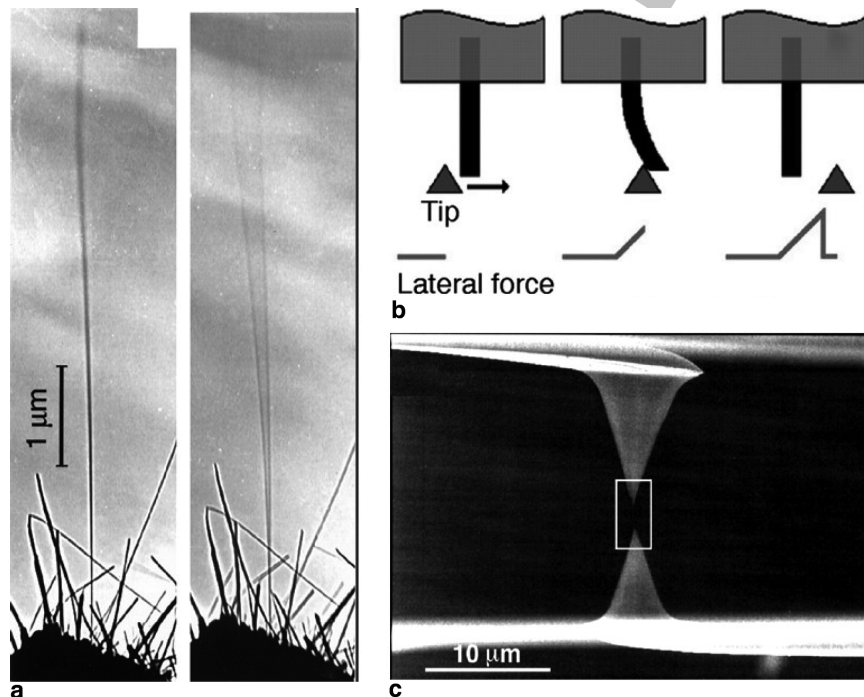

Fig. 11.1 Techniques for mechanical characterization of nanostructures. (**a**) Dynamic responses of an individual CNT to alternate applied potentials, (*left*) absence of a potential, and (*right*) at fundamental mode. Reprinted with permission from Poncharal et al., *Science* 283, 1513 (1999). © 1999, American Association for the Advancement of Science. (**b**) A CNT with one end clamped is deflected by an AFM in lateral force mode. Reprinted with permission from Wong et al., *Science* 277, 1971 (1997). © 1997, American Association for the Advancement of Science. (**c**) An individual MWNT mounted between two opposing AFM tips and stretched uniaxially by moving one tip. Reprinted with permission from Yu et al., *Science* 287, 637 (2000). © 2000, American Association for the Advancement of Science

gold wire, on which a potential was applied. In order to precisely position the wire near the grounded electrode, a special TEM holder with a piezo-driven translation stage and a micrometer-resolution translation stage were used. Application of an AC voltage to the nanotubes caused a time-dependent deflection. The elastic modulus was then estimated from the observed resonance frequencies.

11.3.2 Bending Test

Wong et al. [8] measured the Young's modulus, strength and toughness of MWNTs and SiC nanorods using an AFM in lateral force mode (Fig. 11.1b). The nanostructures were dispersed randomly on a flat surface and pinned to the substrate by means of microfabricated patches. AFM was then used to bend the cantilevered nanostructures transversely. At a certain location along the length of each structure, the force vs. deflection $(F-d)$ curve was recorded to obtain the spring constant of the system. Multiple $F-d$ curves were recorded at various locations along the structure. By considering the nanostructure as a beam, the $F-d$ data were used to estimate the Young's modulus.

Bending of nanostructures resting on a substrate is straightforward to implement. Nevertheless, it cannot eliminate the effect of adhesion and friction from the substrate. To solve the friction issue, Walters et al. [7] suspended the nanotube over a microfabricated trench and bent the nanotube using AFM lateral force mode. Salvetat et al. [38] introduced a similar method by dispersing MWNTs on an alumina ultrafiltration membrane with 200 nm pores. The adhesion between the nanotubes and the membrane was found sufficiently strong to fix the two ends. Using AFM in contact mode, the authors deflected the suspended NTs vertically and measured $F-d$ curves.

11.3.3 Tensile Test

Pan et al. [39] used a stress–strain rig to pull a very long ($\sim$2 mm) MWNT rope containing tens of thousands of parallel tubes. Yu et al. [11] conducted in situ SEM tensile testing of MWNTs with the aid of a nanomanipulator (Fig. 11.1c). A single nanotube was clamped to the AFM tips by localized EBID of carbonaceous material inside the SEM chamber. The experimental setup consisted of three components: a soft AFM probe (force constant less than $0.1\,\text{N}\,\text{m}^{-1}$) as a load sensor, a rigid AFM probe as an actuator, which was driven by a linear motor, and the nanotubes mounted between the two AFM tips. Following the motion of the rigid cantilever, the soft cantilever was bent due to the tensile load, equal to the force applied on the nanotube. The nanotube deformation was recorded by SEM imaging, and the force was measured by recording the deflection of the soft cantilever. The Young's modulus and failure strength of the MWNTs was then obtained using the acquired data.

Although significant progress has been made, the mechanical testing of nanostructures is still quite rudimental. This is mainly due to the lack of control in

experimental conditions and the lack of accuracy in force and displacement measurements. Recent advances in thin film characterization have been remarkable, which have provided some guidance for nanostructure characterization.

11.4 A MEMS-Based Material Testing Stage

MEMS lend themselves naturally to material testing at the nanoscale. These systems consist of a combination of micromachined elements, including strain sensors and actuators, integrated on a single chip. Due to their intermediate size, MEMS serve as an excellent interface between the macro- and nanoworlds. Their extremely fine force and displacement resolution allows accurate measurement and transduction of forces and displacements relevant at the nanometer scale. At the same time, the larger feature sizes and signal levels of MEMS allow handling and addressing by macroscale tools. Furthermore, many of the sensing and actuation schemes are employed in MEMS scale favorably. For example, the time response, sensitivity, and power consumption of electrostatic displacement sensors improve as their dimensions shrink.

Electrostatic comb-drive actuators are often used in MEMS-based testing systems to apply time-dependent forces. van Arsdell and Brown [19] repeatedly stressed a micrometer-scale specimen in bending using a comb-drive actuator fixed to one end of the specimen. This comb-drive actuator swept in an arc-like motion while the opposite end of the specimen was fixed, causing bending stresses in the specimen. The comb-drive was also used to measure displacement, and collect fracture and fatigue data while testing to the point of failure. Kahn et al. [20, 21] determined fracture toughness by controlling crack propagation in a notched specimen using a comb-drive. One end of the specimen was fixed while the other was attached to a perpendicularly oriented comb-drive.

Electrothermal actuation schemes have also been used to apply loading [22,23]. In these actuators, Joule heating induces localized thermal expansion of regions in the actuators and an overall displacement. The resulting strains are often measured using an integrated capacitive sensor and may be verified through digital image correlation.

This section presents a detailed description of the design and modeling of a MEMS-based material testing system [24] for in situ electron microscopy mechanical testing of nanostructures. The device allows for continuous observation of specimen deformation and failure with subnanometer resolution by SEM or TEM while simultaneously measuring the applied load electronically with nano-Newton resolution. First, an analytical model of the thermal actuator used to apply tensile loading is analyzed. It includes an electrothermal analysis to determine the temperature distribution in the actuator, followed by a thermomechanical analysis to determine the resulting displacement. A coupled-field finite element analysis compliments the analytical model. Next, the differential capacitive load sensor is analyzed to determine the output voltage for a given displacement. Finally, a set of design criteria are established based on the analysis as guidelines for design of similar devices. In Sect. 11.5, experimental results using the device are described.

11.4.1 Device Description

The MEMS-based material testing system described here has previously been reported in detail [22, 23, 40]. For the purpose of this chapter, a brief review of the device is presented so that the following experimental results and the way in which they were obtained can be more clearly understood. The device consists of three parts: an actuator, a load sensor, and a gap between them for placement of nanostructures, as shown in Fig. 11.2. The devices were fabricated at MEMSCAP (Durham, NC) using the Multi-User MEMS Processes (MUMPs). Two types of actuators, an electrostatic (comb-drive) actuator [19–21] and an electrothermal actuator [41, 42] were used to apply time-dependent forces or displacements, respectively. The load sensor operates on the basis of differential capacitive sensing [22,23,40]. The sensor displacement is determined by the measured change in capacitance. This displacement is used to compute the applied force based on the known stiffness of the sensor. The design of the actuator and load sensor is described later in detail.

Figure 11.2a shows the entire device with a thermal actuator, load sensor, and space to position the specimen. The electrothermal actuator acts as a "displacement-controlled actuator" in the sense that it applies a prescribed displacement to the specimen regardless of the force required to achieve this displacement (within the functional range of the device). The load sensor is suspended on a set of folded beams of known stiffness and measures the corresponding tensile force applied to the specimen. Figure 11.2b shows an alternative loading stage using an electrostatic rather than a thermal actuator. The electrostatic actuator works as a "force controlled actuator," applying a prescribed force regardless of the resulting displacement (again within a functional range).

The electrothermal actuator has the capability of testing stiff structures, e.g., nanoscale thin films and large diameter NWs, while the comb-drive actuator is better-suited for relatively compliant structures. Both the electrothermal and electrostatic actuators can be readily made using standard microfabrication techniques. The remainder of this section focuses on using the electrothermal actuator as a case study from the perspective of its design, modeling, and integration with the rest of
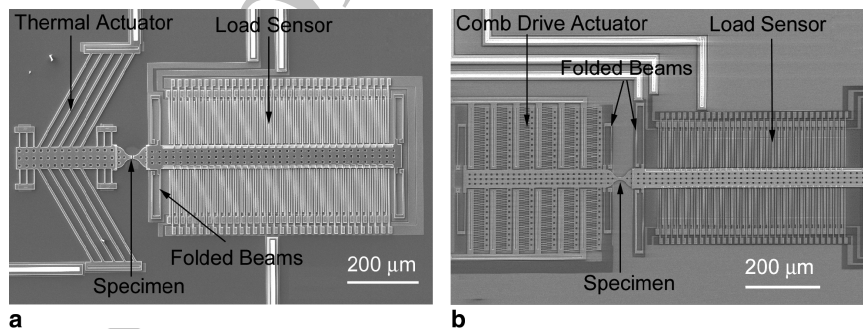

Fig. 11.2 Two variations of the MEMS-based material testing stage. (**a**) "Displacement-controlled" device using a thermal actuator and differential capacitive load sensor. (**b**) "Force-controlled" device using an electrostatic comb-drive actuator and differential capacitive load sensor

the device. Electrostatic actuators have been thoroughly described elsewhere in the literature [43–45].

In this design for in situ SEM testing, 20 devices with different types of actuators and load sensors are arranged on a $10 \times 10 \, \text{mm}^2$ chip. To make electrical connection, there are 100 gold pads fabricated around the periphery of the chip. The chip is glued to the cavity of a ceramic pin grid array package, and the gold pads are wire-bonded to the 100 leads around the cavity as shown in Fig. 11.3a. The corresponding pins in the back of the package make the electric connection to a printed circuit board, which in turn is connected to electronic actuation and measuring instrumentation.

At this size scale, the changes in capacitance of the load sensor are on the order of femtofarads, which is quite challenging to measure. Fortunately, a method to measure charge that mitigates the effect of parasitic capacitance has been developed by the MEMS community [46, 47]. A commercially available integrated circuit based on this method, Universal Capacitive Readout MS3110 (MicroSensors, Costa Mesa, CA), is used here. The MEMS device chip is positioned close to the
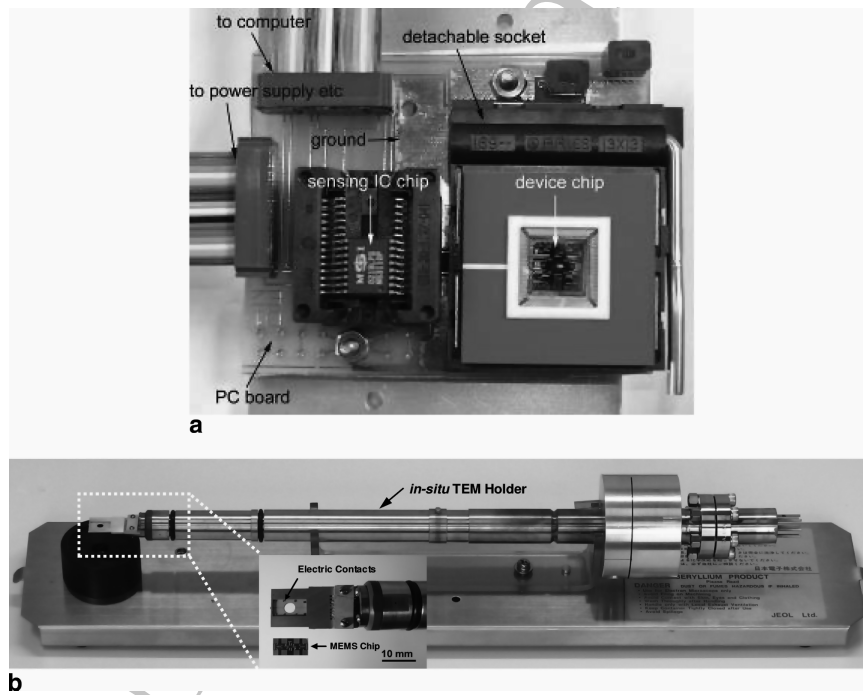

Fig. 11.3 (**a**) Experimental setup for in situ SEM testing. The MEMS device chip is positioned near the MS3110 chip on a printed circuit board. The setup is connected to a power supply, a digital multimeter, and a computer outside the SEM by means of a chamber feedthrough. (**b**) The upper image shows the In situ TEM holder containing a feedthrough, the lower one shows the magnified view of the eight electric contact pads [36] along with a $5 \times 10 \, \text{mm}$ MEMS chip. In an actual experiment, the MEMS chip is flipped, placed in the TEM holder, and fixed by the left and right clamps

integrated sensing chip on the circuit board to minimize amplified electromagnetic interference (Fig. 11.3a). The output voltage of the integrated circuit is proportional to the capacitance change.

In addition to the in situ SEM measurements reported here, this device has the potential to impact other nanoscale characterization techniques. For instance, in situ TEM testing of nanostructures is possible with the addition of a microfabricated window beneath specimen gap to allow the imaging beam to pass through the device substrate. The major challenge here is to etch the window, from the back of the silicon wafer, without damaging the previously fabricated structures. This was accomplished by deep reactive ion etching of the window before releasing the devices [22, 23]. Figure 11.3b shows a MEMS chip (5×10 mm) containing four MEMS devices. The two devices in the center are used for in situ TEM testing, while the other two devices are used for calibration purposes. The chip has eight contact pads for electrical actuation/sensing. The chip is designed to be directly mounted on a specially designed TEM holder containing a feed-through and interconnects to electrically operate the devices (Fig. 11.3b) [22, 23]. In this case, the sensing integrated circuit chip (MS3110) used in the capacitance measurement is located outside of the TEM.

11.4.2 Electrothermal Actuator Design

Electrothermal actuation complements electrostatic schemes as a compact, stable, high-force actuation technique [48]. Various forms of thermal actuators have been employed in systems ranging from linear and rotary microengines [49] to two-dimensional nanoscale positioners [50], optical benches [51], and instrumentation for material characterization [52]. By incorporating compliant mechanisms, larger displacements can be achieved [50].

Modeling of the thermal actuators generally takes one of two approaches:

1. A sequential electrothermal and thermostructural analysis [53–55]
2. A completely coupled three-dimensional FEA [56]

Additional analyses include characterization of the temperature-dependent electrothermal properties [48–56] of these devices. A schematic of the thermal actuator analyzed in this section is shown in Fig. 11.4. The thermal actuator consists of a series of inclined polysilicon beams supporting a free-standing shuttle. One end of each of the inclined beams is anchored to the substrate while the other end connects to the shuttle. Thermal expansion of the inclined beams, induced by Joule heating, causes the shuttle to move forward. The heating is the result of current flowing through the beams because of a voltage bias applied across the two anchor points [57]. Modeling of these actuators requires a two-step analysis; first an electrothermal analysis to determine the temperature distribution in the device, followed by a thermostructural analysis to determine the resulting displacement field.
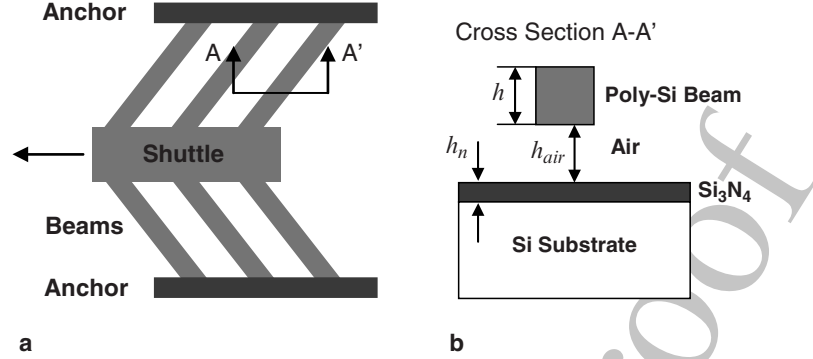
Fig. 11.4 (**a**) Schematic of the thermal actuator. (**b**) Cross section of a single beam suspended over the substrate

An electrothermal model of the device is developed to determine the temperature distribution as a function of the applied voltage. This is highly dependent upon the operating environment. When operating in air, the dominant heat transfer mechanism is heat conduction between the actuator and substrate through the air-filled gap between them [54, 55, 57]. In this scenario, the governing equation is

$$k_p \frac{\mathrm{d}^2 T}{\mathrm{d}x^2} + J^2 \rho = \frac{S}{h} \frac{T - T_\mathrm{s}}{R_\mathrm{T}}, \tag{11.1}$$

where k_p and ρ are the thermal conductivity and resistivity of the polysilicon beams, respectively; T is the temperature; J the current density; $S = (h/w)((2h_{air}/h) + 1) + 1$ is a shape factor accounting for the effect of element shape on heat conduction to the substrate; $R_\mathrm{T} = (h_{\mathrm{air}}/k_{\mathrm{air}}) + (h_\mathrm{n}/k_\mathrm{n}) + (h_\mathrm{s}/k_\mathrm{s})$ is the thermal resistance between the polysilicon beam and substrate; h and w are the thickness and width of a single beam, respectively; h_{air} is the gap between the beam and silicon nitride layer on the substrate; h_n is the thickness of the silicon nitride; h_s is the representative thickness of the substrate; k_{air}, k_n, k_s are the thermal conductivities of air, silicon nitride, and the substrate, respectively; and T_s is the temperature of the substrate.

The thermal conductivities k_p and k_{air} are both temperature dependent. However, the assumption of a constant k_p yields results similar to those using a temperature-dependent value of k_p [53]. Assuming a constant k_p and temperature dependent k_{air}, the finite difference method is implemented to solve (11.1) by writing the second-order differential equation in the form $\mathrm{d}^2 T/\mathrm{d}x^2 = b(x, T)$, and approximating it as

$$\frac{\mathrm{d}^2 T}{\mathrm{d}x^2} \approx \frac{1}{(\Delta x)^2}(T_{i+1} - 2T_i + T_{i-1}). \tag{11.2}$$

Figure 11.5a shows the steady-state temperature profile obtained for a two-leg (one pair of inclined beams) thermal actuator operating in air. The temperature of the shuttle is significantly lower than that of each of the beams. This is due to the relatively low current density in the shuttle, resulting in a lower rate of heat generation
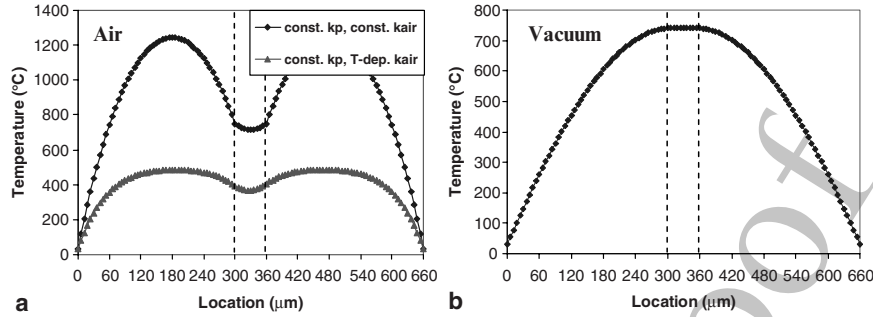
Fig. 11.5 Steady-state temperature profile (with respect to the substrate) along a pair of inclined beams and the shuttle while operated (**a**) in air for both constant and temperature-dependent values of k_{air} and (**b**) in vacuum with an input current of 10 mA. In both cases, locations 0–300 μm and 360–660 μm correspond to the thermal beams while the center region is the shuttle between the beams. The beams are anchored to the substrate at 0 and 660 μm. In air, the highest temperature occurs in the beams

as compared to that of the beams. Furthermore the relatively large area of the shuttle results in greater heat dissipation through the air as compared to the beams.

The thermal conductivity of air has a significant effect on the actuator behavior [54]. This strong dependence is clearly seen in the two curves plotted in Fig. 11.5a – in one case (purple curve) temperature dependence of thermal conductivity of air is taken into account. k_{air} increases with temperature, increasing the heat flow between the beams and shuttle and the substrate. Consequently the temperature of the beams and shuttle is lower for a given current flow. It is clear that decreasing heat conduction through the air increases the temperature of the beams. Ultimately, operation in vacuum maximizes the beam temperature for a given current flow, making the device more efficient.

In contrast, heat dissipation by conduction through the anchors to the substrate dominates in vacuum [54, 57]. Assuming each beam is thermally independent, an electrothermal model based on a single beam is presented [54]. Heat transfer within the beam is treated as a one-dimensional problem since the length dimension is significantly larger than either of the cross-sectional dimensions. To analyze the case where the thermal actuator operates in vacuum, the term for heat conduction through the air is removed from (11.1),

$$k_{\mathrm{p}}\frac{\mathrm{d}^2T}{\mathrm{d}x^2} + J^2\rho = 0. \tag{11.3}$$

Figure 11.5b shows that the highest temperature now occurs in the shuttle rather than in the beams. Here the temperature depends mostly upon the distance from the anchor points which are now assumed to be the only source of heat dissipation. Since the shuttle is furthest from the anchors, it reaches the highest temperature. With the temperature distribution known from this electrothermal analysis, the thermomechanical behavior of the actuator is modeled to determine the resulting displacement [22, 23].

AQ: As per instruction from Springer, all figures were converted to b/w, but color is mentioned in the text. Please modify the text accordingly.

While the displacement of the actuator in vacuum is easily characterized experimentally [40], the temperature distribution is more difficult to obtain. Therefore a coupled-field simulation is particularly necessary. Coupled analysis also helps to assess the temperature at the actuator–specimen interface and to examine the effectiveness of the thin heat sink beams in controlling the temperature increase of the specimen during actuation.

The MEMS-based tensile stage is intended to operate within the SEM or TEM. Thus the following finite element electrothermal analysis is carried out for the case where the device operates in vacuum. The actuation voltage applied across the anchor points serves as the input while the output includes both the actuator temperature and displacement fields. Displacements at the anchor points are held fixed as applied mechanical boundary conditions. The thermal boundary conditions dictate a constant temperature at the anchors.

Figure 11.6a, b depict the temperature and displacement fields observed in the thermal actuator for an actuation voltage of 1 V. As previously mentioned, heat dissipation through the anchors is the dominant dissipation mechanism. Since the shuttle is furthest from the anchors, the highest temperature occurs in the shuttle. Due to the nonuniformity of the temperature distribution, the displacement is also nonuniform.
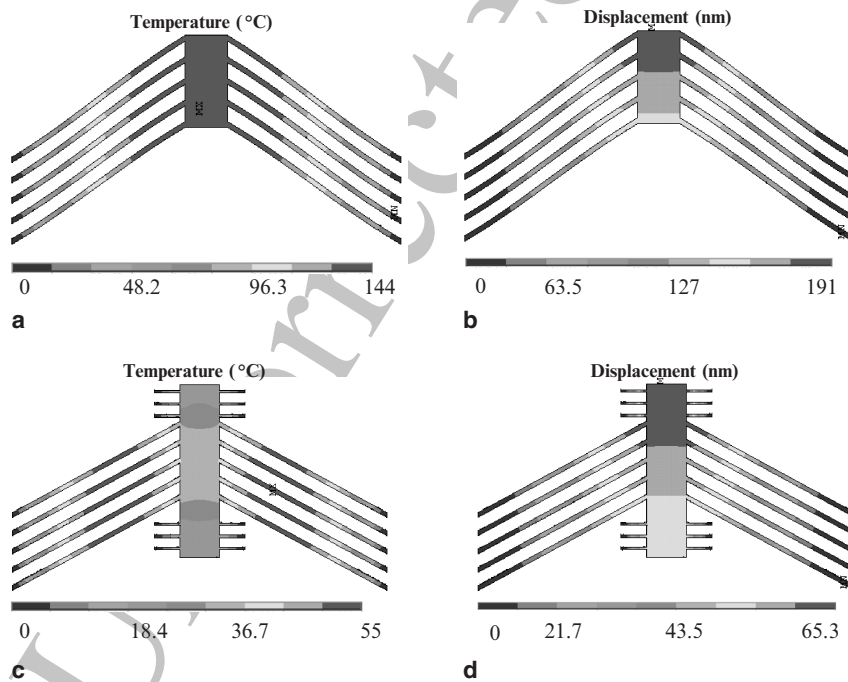

Fig. 11.6 (**a**) Temperature increase (°C) and (**b**) displacement field (nm) in the thermal actuator. The displacement component plotted is in the shuttle axial direction. (**c**) Temperature (°C) and (**d**) displacement field (nm) in the thermal actuator with three pairs of heat sink beams at the specimen end. In this analysis, the heat sink beams are 40 μm in length and 4-μm wide with 16 μm spacing between them. ANSYS Multiphysics, version 6.1 was used for this analysis

Heating of the specimen during actuation is unavoidable as a result of the increased temperature of the shuttle to which the sample is attached. However, this effect is minimized with the addition of a series of heat sink beams running between the shuttle and substrate near the shuttle-specimen interface as shown in Fig. 11.6c, d. To avoid out-of-plane bending, another three pairs of heat sink beams are placed at the opposite end of the shuttle. Comparing the two cases – with and without heat sink beams – it is found that similar displacement can be obtained at shuttle end for significantly smaller temperatures at the shuttle–specimen interface with heat sink beams. For highly temperature sensitive materials, the problem of specimen heating can be further mitigated with the addition of a thermal isolation layer between the actuator and specimen following the custom microfabrication process [57].

The thermal actuator is calibrated experimentally to verify the analytical and FEA models described above. Figure 11.7 [40] shows a comparison of experimentally measured results with the analytical and FEA predictions of the actuator displacement for a given current input. The displacement of the actuators was measured with a SEM [22], having spatial resolution of better than 5 nm. Using the analytical model, the displacement is computed based on experimentally measured temperatures in the actuator [40]. In order to obtain the current, resistance of the actuator is computed using the output temperature and a value of resistivity corresponding to the average temperature of the device.

The models agree well with the experimentally measured actuator displacements as shown in Fig. 11.7. This suggests that the models are useful in predicting the behavior of thermal actuators of other geometry. At large currents (more than ~12 mA), both analytical and FEA models deviate slightly from the experimental results. This can be explained largely by inaccuracies in material parameters such as resistivity and thermal conductivity at high temperatures [48, 54]. Furthermore, the microstructure of polysilicon starts getting transformed at these high current levels and elevated temperatures [40].
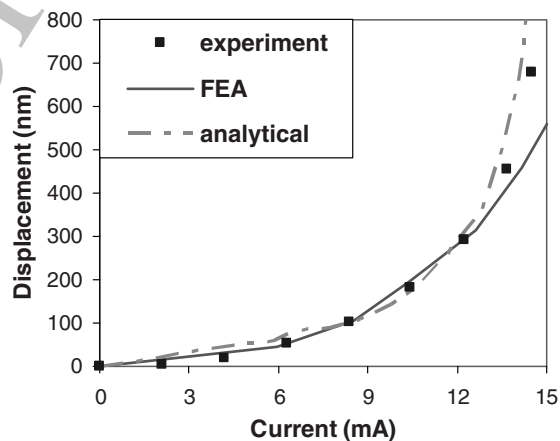
Fig. 11.7 Comparison of the displacements at the actuator–specimen interface as predicted by the analytical and FEA models and measured experimentally. Displacement is plotted as a function of the input current

11.4.3 Load Sensor Design

The load sensing mechanism consists of a differential capacitive displacement sensor suspended on a set of elastic members of known stiffness. By calibrating the stiffness of the elastic members [22, 23], the load is computed based on the measured displacement. The differential capacitive displacement sensor [45, 46, 58] is chosen for its sensitivity and linear behavior over a range of displacements appropriate for tensile testing of nanostructures.

The differential capacitive sensor is comprised of a movable rigid shuttle with electrodes (or "fingers") pointing outward as shown schematically in Fig. 11.8b [22]. These fingers are interdigitated between pairs of stationary fingers (Fig. 11.8b) fixed to the substrate. Under load-free condition each movable finger sits in the middle of two stationary fingers. Each set of fingers (one movable and two stationary ones on the sides) forms two capacitors. The entire capacitance sensor is equivalent to two combined capacitances, C_1 and C_2, as shown in Fig. 11.8a.

$$C_1 = C_2 = C_0 = \varepsilon N \frac{A}{d_0}(1+f), \qquad (11.4)$$

where ε is the electric permittivity; N is the number of unit movable fingers; A and d_0 are the area of overlap and initial gap, respectively between the movable finger and each stationary finger; and $f = 0.65 d_0/h$ is the fringing field correction factor with h being the beam height [59].
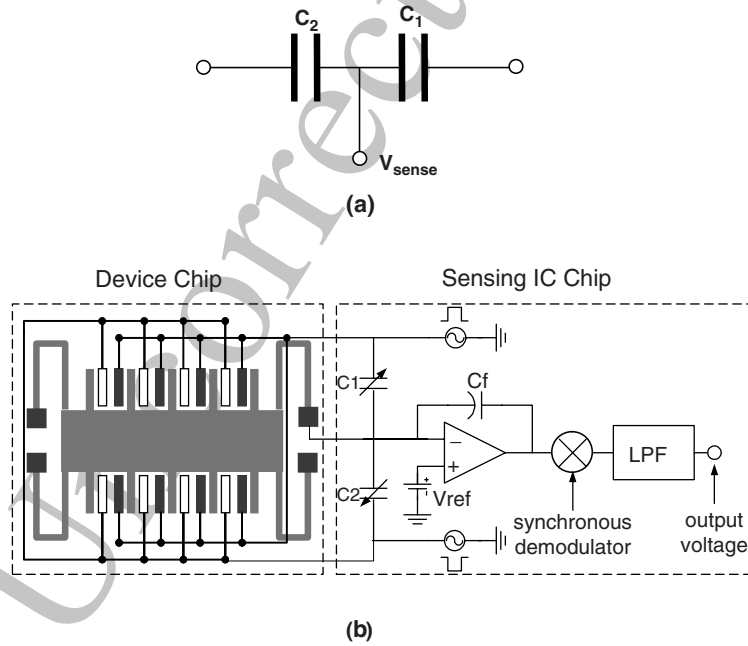

Fig. 11.8 (**a**) A simple model of the differential capacitor. (**b**) Double chip architecture used for measuring capacitance change. The capacitance change is proportional to the output-voltage change

The movable fingers are attached to the folded beams via the rigid movable shuttle, such that the displacement of shuttle and the beams is the same. This displacement yields a change in capacitance given by,

$$\Delta C = C_1 - C_2 = N\varepsilon A \left(\frac{1}{d_0 - \Delta d} - \frac{1}{d_0 + \Delta d} \right) \approx \frac{2N\varepsilon A}{d_0^2} \Delta d, \quad (11.5)$$

where Δd is the displacement of the load sensor. Note that the fringing effect factor cancels. For displacements Δd with 50% of the initial gap d_0, the capacitance changes approximately linearly with the sensor displacement. This relatively large range of linear sensing is a major advantage of differential capacitance sensing over direct capacitance sensing which uses a single fixed beam for each movable beam.

A variety of circuit configurations may be used in measuring capacitance [45,46]. Figure 11.8b shows schematically the charge sensing method used in the device. This method mitigates the effects of parasitic capacitances that generally occur in electrostatic MEMS devices. Here the change in output voltage ΔV_{sense} is proportional to the capacitance change [22],

$$\Delta V_{\text{sense}} = \frac{V_0}{C_{\text{f}}} \Delta C, \quad (11.6)$$

where V_0 is the amplitude of an AC voltage signal applied to the stationary fingers and C_{f} the feedback capacitor as shown in Fig. 11.8b.

Minimizing stray capacitance and electromagnetic interference is critical in high resolution capacitance measurements. In this case, integrating the MEMS differential capacitor and sensing electronics on a single chip minimizes these effects, allowing detection of changes in capacitance at the atto-Farad level [46]. However, this greatly increases the fabrication complexity. The double chip architecture depicted in Fig. 11.8 is an alternative to the single chip scheme. Here the MEMS-based system is fabricated on one chip while a commercial integrated circuit chip (for e.g., Universal Capacitive Readout MS3110, Microsensors, Costa Mesa, CA) is used to measure changes in capacitance. Both chips are housed on a single printed circuit board.

11.4.4 System Analysis

With the mechanical response of the thermal actuator known for a given current input, it is now possible to formulate a set of equations governing the behavior of the entire device [40]. A lumped model of the entire device is shown in Fig. 11.9. Here K_S is the stiffness of the tensile specimen, K_{LS} is the stiffness of the load sensor corresponding to the folding beams by which it is suspended, K_{TA} is the stiffness of the thermal actuator computed before, and U_{LS} is the displacement of the load sensor. The central shuttle is assumed to be rigid.
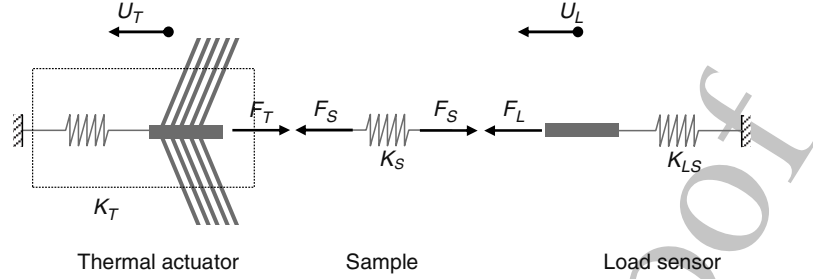
Fig. 11.9 Lumped model of the entire tensile loading device with internal forces and displacements shown in free body form

The following are the governing equations for the lumped system [40]:

$$
\begin{aligned}
\Delta U_{\text{S}} &= U_{\text{TA}} - U_{\text{LS}} \\
U_{\text{TA}} &= \frac{2m\alpha\Delta T E A s - F_{\text{TA}}}{K_{\text{TA}}} \\
F_{\text{TA}} &= F_{\text{S}} = F_{\text{LS}} \\
F_{\text{S}} &= K_{\text{S}}\Delta U_{\text{S}} \\
F_{\text{LS}} &= K_{\text{LS}}U_{\text{LS}}
\end{aligned}
\tag{11.7}
$$

where $s = \sin\theta$ and ΔU_{S} is the elongation of the specimen, E is the Young's modulus, α is the coefficient of thermal expansion of the beam material, and m is the number of pairs of beams. Solving the system of equations (11.7), one obtains the displacement of the thermal actuator U_{TA}, the tensile force on the specimen F_{S}, the elongation of the specimen ΔU_{S}, and the corresponding displacement of the load sensor U_{LS} as,

$$
\begin{aligned}
U_{\text{TA}} &= \frac{2m\alpha\Delta T E A s}{(K_{\text{TA}} + K_{\text{TA}}K_{\text{LS}}/K_{\text{S}} + K_{\text{LS}})} + \frac{2m\alpha\Delta T E A s}{(K_{\text{TA}} + K_{\text{S}} + K_{\text{TA}}K_{\text{S}}/K_{\text{LS}})} \\
F_{\text{S}} &= \frac{2m\alpha\Delta T E A s}{(K_{\text{TA}}/K_{\text{S}} + 1 + K_{\text{TA}}/K_{\text{LS}})} \\
\Delta U_{\text{S}} &= \frac{2m\alpha\Delta T E A s}{(K_{\text{TA}} + K_{\text{S}} + K_{\text{TA}}K_{\text{S}}/K_{\text{LS}})} \\
U_{\text{LS}} &= \frac{2m\alpha\Delta T E A s}{(K_{\text{TA}} + K_{\text{TA}}K_{\text{LS}}/K_{\text{S}} + K_{\text{LS}})}
\end{aligned}
\tag{11.8}
$$

where A is the cross-sectional area of the beam. These represent the critical parameters in obtaining force–displacement data using the MEMS-based tensile testing device.

Considering the above analyses, the following design criteria are set to achieve an effective and reliable material testing system:

1. Large load sensor displacements to maximize load resolution
2. Low temperature at the actuator–specimen interface to avoid artificial heating of the specimen
3. Displacement-controlled testing i.e., the stiffness of the thermal actuator is significantly higher than that of the specimen and load sensor

The specimen stiffness, failure load, and elongation at failure (ΔU_S) dictate the choice of actuator geometry and the number and dimensions of the beams. Consequently optimization of the device design requires some preliminary knowledge of the specimen behavior as is customary in experimental mechanics.

11.5 Experimental Results

11.5.1 Device Calibration

To obtain the relationship between the measured capacitance and corresponding displacement, an identical device with a solid connection between the actuator and load sensor (i.e., no gap for specimen mounting) was fabricated on the same chip. Real time high-resolution images were employed to calibrate the capacitance measurements [23] within a field emission SEM (Leo Gemini 1525). The device was actuated with a series of stepwise increasing voltages, applied sequentially in six ON–OFF cycles. A high contrast feature on the movable shuttle was selected for capturing images at high magnification ($\times$183k). The device state during successive ON–OFF actuation cycles was captured in a single SEM image, as shown in Fig. 11.10a. Simultaneously, the output voltage V_{sense} was recorded by a digital
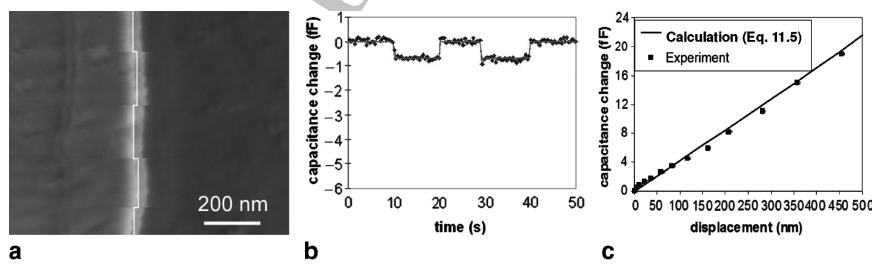

Fig. 11.10 Calibration of the load sensor showing the relationship between the capacitance change and measured displacement from SEM images at a series of actuation voltage. (**a**) and (**b**) Signatures when actuator is at 2 V; reference feature in the SEM image showing a motion of 15 nm due to four ON–OFF actuations (**a**), and plot corresponding to a 0.7 fF capacitance change resulting from the same actuation (**b**). Both raw data and fitted data are shown in the plot of capacitance measurements. (**c**) Plot of displacement vs. capacitance change resulting from the calibration

multimeter and converted to the capacitance change using (11.6). Figure 11.10b shows the raw data of V_{sense} at an actuation voltage of 5.5 V.

Figure 11.10c shows a plot of experimental data correlating the displacements/loads and the capacitance changes (in dots). The relationship between displacement and capacitance change as predicted in (11.5) is plotted in solid line [40] is evident that the experimental data agrees with the predictions very well. The achievable resolution of the measured capacitance change is 0.2 fF and the corresponding displacement resolution is 3 nm.

Another important step in the calibration procedure is the accurate measurement of the load sensor stiffness. This can be accomplished in one of two ways (1) by resonance methods, a common procedure in MEMS research [22] or (2) by identifying the Young's modulus of the material, E, and then using FEA with accurate metrology to determine the structural stiffness. For the parallel beams in the load sensor, the resonating voltage cannot be larger than the *pull-in* voltage so the second methodology is employed. Since the load sensor and actuator are comprised of the same material, the accuracy of the load sensor stiffness prediction is assessed by determining the comb-drive actuator stiffness using the resonance method and then comparing this result with the one calculated by FEA. In the resonance method, the stiffness is calculated by $K = (2\pi f_r)^2 (M_s + 0.3714 M_b)$ [22], where f_r is the resonant frequency, M_s and M_b the masses of the shuttle and the folded beams, respectively. For the comb-drive actuator, we measured a resonant frequency of 17.2 ± 0.1 kHz. The corresponding stiffness is 20.3 N m^{-1}, while the computed stiffness based on the *measured* folded beam geometry, using $E = 170$ GPa [60], was 20.7 N m^{-1}. This clearly shows that the stiffness computed based on the fabricated geometry and the known value of Young's modulus is in good agreement with that identified from the resonance experiment. Following this procedure, the stiffness of the load sensor designed for the testing CNTs was computed to be 11.8 N m^{-1}, which corresponds to a load resolution of 35 nN [22]. Likewise, the stiffness of the load sensor designed for testing NWs was 48.5 N m^{-1} with a load resolution of 145 nN.

11.5.2 Tensile Tests of Co-Fabricated Polysilicon Thin Films

The size and fragile nature of nanostructures demands specialized techniques for preparation and mounting on the aforementioned MEMS device. Thin films may be co-fabricated with the MEMS device. This eliminates any handling or nanomanipulation of the specimen. For example, freestanding polysilicon films were co-fabricated with the MEMS device between the actuator and the load sensor (Fig. 11.11a) [23]. Due to limitations in the resolution of the photolithography used to make the devices, the initial specimen width could not be made thinner than approximately 2 μm. To reduce this dimension, the polysilicon specimen was further machined by focused ion beam (FIB) down to 350–450 nm.

Thin film specimens co-fabricated with the MEMS device were then tested in in situ SEM. The results of a tensile test of a polysilicon specimen prepared as
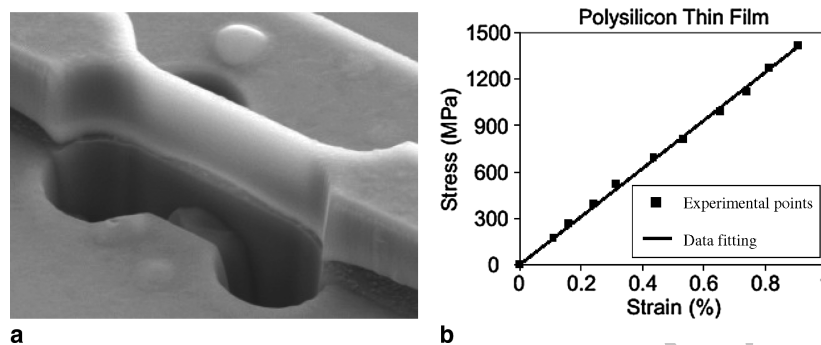
Fig. 11.11 (**a**) A tensile specimen of polysilicon thin film co-fabricated with the MEMS device and further thinned by FIB machining. (**b**) Measured stress–strain data [40]

described above are shown in Fig. 11.11b. Here the stress–strain curve shows strong linearity with a Young's modulus of 156 ± 17 GPa [40]. This result is consistent with other reported values for polysilicon films [60–62], which provides confidence in the overall experimental protocol and data reduction.

11.5.3 Tensile Tests of Nanowires

It is known that nanowires posses a relatively large surface area-to-volume ratio. Consequently interfaces, interfacial energy, and surface topography play an increasingly important role in their deformation and failure processes. In larger structures, generation and propagation of defects dictate material behavior. As grain sizes or structural dimensions fall below 50–100 nm, interatomic reorganization near surfaces gain influence over bulk material behavior. Therefore understanding the deformation and fracture mechanics of these new one-dimensional nanostructures is essential.

Testing of individual nanowires and nanotubes with the MEMS device as described above may be achieved either by growing the specimen across the gap between actuator and load sensor or by placement of the specimen in the device by nanomanipulation [23]. The latter procedure involves use of a nanomanipulator operated inside an SEM to pick up and place the individual nanostructure across the gap, followed by EBID of platinum to weld the ends.

In situ SEM tensile tests of silver nanowires using the MEMS device were performed to identify the material stress–strain behavior and failure. Figure 11.12a shows sequential SEM images obtained during the testing of a silver nanowire. The nanowire specimen began to deform at an actuation voltage of 0.8 V and failed at 6.6 V. The strain–stress data, shown in Fig. 11.12b, reveal key features. The nanowires were stressed to about 2–2.5 GPa, which is significantly higher than the tensile strength (1.7 GPa) of bulk silver [63], before necking. This phenomenon,
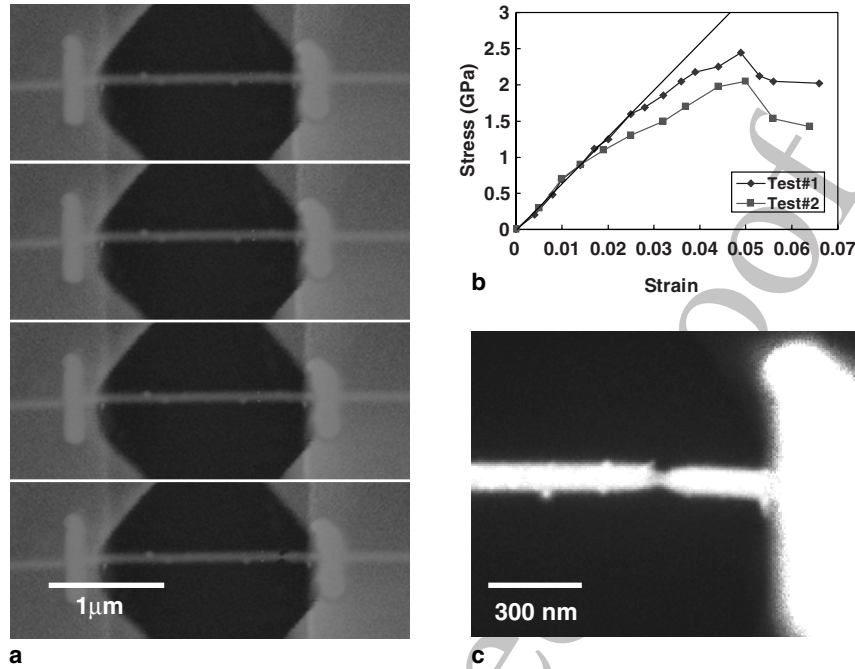
Fig. 11.12 In situ SEM tensile testing of a silver nanowire. (**a**) Sequential SEM images of a tensile loading process. The nanowire is 1.9 μm in length and 100 nm in width. (**b**) The strain–stress data, and (**c**) the fracture surface of the nanowire showing the necking

which is attributed to the absence of defects and high stress threshold for the nucleation of defects [64, 65], agrees with the hypothesis that the strength of the material increases as the specimen's characteristic dimension decreases. The nanowires underwent large localized plastic deformation leading to necking and fracture (Fig. 11.12c). A failure strain of about 6% was identified in the experiment. It is interesting to note that the softening regime captured in the experiments was possible only because of the displacement control characteristic of the thermal actuator.

11.6 Summary

The first 1D nanostructure was synthesized more than a decade ago. Since then, a number of nanodevices using these nanostructures have been developed. Mechanical characterizations at the nanoscale become an important activity to predict and assess device integrity and durability as well as to gain fundamental understanding of deformation processes at the nanoscale. Most of the developed nanomechanincal testing techniques did not possess a well-controlled loading condition and electronic load–displacement measurement. As such, in situ mechanical testing relied

on indirect measurement of load through imaging of deforming beams. This chapter described the modeling and analysis involved in the design of a MEMS-based material testing system, which allows *simultaneous* load–displacement measurements combined with *real-time high resolution* SEM or TEM imaging of the specimen without the need for shifting the imaging beam. The system uses a thermal actuator to apply load and a differential capacitive displacement sensor, of known stiffness, to electronically measure the applied load. An analytical model of the thermal actuator involving electro-thermal-mechanical analysis was developed to determine the temperature distribution in the actuator, displacement and force fields. A coupled-field FEA was used to verify the analytical model and obtained further insight on the field variables. A set of design criteria were then established. Finally, examples of application of the MEMS-based material testing system to characterize co-fabricated polysilicon thin films and Ag nanowires were presented.

References

1. Iijima S (1991) Nature 354(6348):56
2. Yakobson BI, Avouris P (2001) Carbon Nanotubes. Topics in Applied Physics, vol. 80. Springer, Berlin, p. 287
3. Fennimore AM, Yuzvinsky TD, Han WQ, Fuhrer MS, Cumings J, Zettl A (2003) Nature 424(6947):408
4. Dalton AB, Collins S, Munoz E, Razal JM, Ebron VH, Ferraris JP, Coleman JN, Kim BG, Baughman RH (2003) Nature 423(6941):703
5. Treacy MMJ, Ebbesen TW, Gibson JM (1996) Nature 381(6584):678
6. Poncharal P, Wang ZL, Ugarte D, de Heer WA (1999) Science 283(5407):1513
7. Walters DA, Ericson LM, Casavant MJ, Liu J, Colbert DT, Smith KA, Smalley RE (1999) Appl. Phys. Lett. 74(25):3803
8. Wong EW, Sheehan PE, Lieber CM (1997) Science 277(5334):1971
9. Shen WD, Jiang B, Han BS, Xie SS (2000) Phys. Rev. Lett. 84(16):3634
10. Li XD, Hao HS, Murphy CJ, Caswell KK (2003) Nano Lett. 3(11):1495
11. Yu MF, Lourie O, Dyer MJ, Moloni K, Kelly TF, Ruoff RS (2000) Science 287(5453):637
12. Tsuchiya T, Tabata O, Sakata J, Taga Y (1998) J. Microelectromech. Syst. 7(1):106
13. Greek S, Ericson F, Johansson S, Furtsch M, Rump A (1999) J. Micromech. Microeng. 9(3):245
14. Chasiotis I, Knauss WG (2002) Exp. Mech. 42(1):51
15. Hugo RC, Kung H, Weertman JR, Mitra R, Knapp JA, Follstaedt DM (2003) Acta Mater. 51(7):1937
16. Robertson IM, Lee TC, Birnbaum HK (1992) Ultramicroscopy 40(3):330
17. Haque MA, Saif MTA (2002) Exp. Mech. 42(1):123
18. Haque MA, Saif MTA (2004) Proc. Natl. Acad. Sci. USA 101(17):6335
19. van Arsdell WW, Brown SB (1999) J. Microelectromech. Syst. 8(3):319

20. Osterberg PM, Senturia SD (1997) J. Microelectromech. Syst. 6(2):107
21. Kahn H, Ballarini R, Mullen RL, Heuer AH (1999) Proc. R. Soc. Lond. A Math. Phys. Eng. Sci. 455(1990):3807
22. Zhu Y, Moldovan N, Espinosa HD (2005) Appl. Phys. Lett. 86(1):013506
23. Zhu Y, Espinosa HD (2005) Proc. Natl. Acad. Sci. USA 102(41):14503
24. Lu JP (1997) Phys. Rev. Lett. 79(7):1297
25. Falvo MR, Clary GJ, Taylor RM, Chi V, Brooks FP, Washburn S, Superfine R (1997) Nature 389(6651):582
26. Williams PA, Papadakis SJ, Falvo MR, Patel AM, Sinclair M, Seeger A, Helser A, Taylor RM, Washburn S, Superfine R (2002) Appl. Phys. Lett. 80(14):2574
27. Cumings J, Zettl A (2000) Science 289(5479):602
28. Smith PA, Nordquist CD, Jackson TN, Mayer TS, Martin BR, Mbindyo J, Mallouk TE (2000) Appl. Phys. Lett. 77(9):1399
29. Chen XQ, Saito T, Yamada H, Matsushige K (2001) Appl. Phys. Lett. 78(23):3714
30. Hughes MP, Morgan H (1998) J. Phys. D Appl. Phys. 31(17):2205
31. Huang Y, Duan XF, Wei QQ, Lieber CM (2001) Science 291(5504):630
32. Fujiwara M, Oki E, Hamada M, Tanimoto Y, Mukouda I, Shimomura Y (2001) J. Phys. Chem. A 105(18):4383
33. Rao SG, Huang L, Setyawan W, Hong SH (2003) Nature 425(6953):36
34. Piner RD, Zhu J, Xu F, Hong SH, Mirkin CA (1999) Science 283(5402):661
35. Dai HJ (2000) Phys. World 13(6):43
36. Kong J, Soh HT, Cassell AM, Quate CF, Dai HJ (1998) Nature 395(6705):878
37. He RR, Gao D, Fan R, Hochbaum AI, Carraro C, Maboudian R, Yang PD (2005) Adv. Mater. 17(17):2098
38. Salvetat JP, Briggs GAD, Bonard JM, Bacsa RR, Kulik AJ, Stockli T, Burnham NA, Forro L (1999) Phys. Rev. Lett. 82(5):944
39. Pan ZW, Xie SS, Lu L, Chang BH, Sun LF, Zhou WY, Wang G, Zhang DL (1999) Appl. Phys. Lett. 74(21):3152
40. Zhu Y, Corigliano A, Espinosa HD (2006) J. Micromech. Microeng. 16:242
41. Chu L, Que L, Gianchandani Y (2002) J. Microelectromech. Syst. 11:489
42. Fischer E, Labossiere P (2002) In: Proceedings of the SEM Annual Conference on Experimental and Applied Mechanics, Milwaukee, WI
43. Saif MTA, MacDonald NC (1996) Sens. Actuators A 52:65
44. Tang WC, Nguyen TCH, Howe RT (1989) Sens. Actuators A 20:53
45. Legtenberg R, Groeneveld AW, Elwenspoek M (1996) J. Micromech. Microeng. 6:320
46. Senturia SD (2002) Microsystem Design. Kluwer, Boston
47. Boser PE (1997)In: Proc. Transducers, Chicago, IL
48. Geisberger AA, Sarkar N, Ellis M, Skidmore GD (2003) J. Microelectromech. Syst. 12:513
49. Park JS, Chu LL, Oliver AD, Gianchandani YB (2001) J. Microelectromech. Syst. 10:255
50. Chu LL, Gianchandani YB (2003) J. Micromech. Microeng. 13:279
51. Pai MF, Tien NC (2000) Sens. Actuators A 83:237
52. Kapels H, Aigner R, Binder J (2000) IEEE Trans. Electron. Devices 47:1522
53. Chiao M, Lin LW (2000) J. Microelectromech. Syst. 9:146
54. Lott CD, Mclain TW, Harb JN, Howell LL (2002) Sens. Actuators A 101:239
55. Huang QA, Lee NKS (1999) Microsyst. Technol. 5:133
56. Mankame ND, Ananthasuresh GK (2001) J. Micromech. Microeng. 11:452
57. Que L, Park JS, Gianchandani YB (2001) J. Microelectromech. Syst. 10:247
58. Boser BE, Howe RT (1996) IEEE J. Solid-State Circuits 31:366
59. Huang JM, Liew KM, Wong CH, Rajendran S, Tan MJ, Liu AQ (2001) Sens. Actuators A 93:273
60. Espinosa HD, Peng B, Prorok BC, Moldovan N, Auciello O, Carlisle JA, Gruen DM, Mancini DC (2003) J. Appl. Phys. 94:6076
61. Sharpe WN, Jackson KM, Hemker KJ, Xie Z (2001) J. Microelectromech. Syst. 10:317

62. Corigliano A, De Masi B, Frangi A, Comi C, Villa A, Marchi M (2004) J. Microelectromech. Syst. 13:200
63. Giancoli D (2000) Physics for Scientists and Engineers, 3rd edn. Prentice-Hall, Upper Saddle River
64. Espinosa HD, Prorok B, Peng B (2004) J. Mech. Phys. Solids 52:667
65. Barber A, Kaplan-Ashiri I, Cohen S, Tenne R, Wagner H (2005) Compos. Sci. Technol. 65:2380